

# Accepted Manuscript

Prussian blue nanocubes supported on graphene foam as superior binder-free anode of lithium-ion batteries

Meizhou Zhu, Hu Zhou, Jinxiao Shao, Jianhui Feng, Aihua Yuan



PII: S0925-8388(18)31255-6

DOI: [10.1016/j.jallcom.2018.03.378](https://doi.org/10.1016/j.jallcom.2018.03.378)

Reference: JALCOM 45608

To appear in: *Journal of Alloys and Compounds*

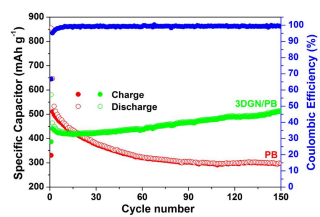
Received Date: 16 November 2017

Revised Date: 27 March 2018

Accepted Date: 28 March 2018

Please cite this article as: M. Zhu, H. Zhou, J. Shao, J. Feng, A. Yuan, Prussian blue nanocubes supported on graphene foam as superior binder-free anode of lithium-ion batteries, *Journal of Alloys and Compounds* (2018), doi: 10.1016/j.jallcom.2018.03.378.

This is a PDF file of an unedited manuscript that has been accepted for publication. As a service to our customers we are providing this early version of the manuscript. The manuscript will undergo copyediting, typesetting, and review of the resulting proof before it is published in its final form. Please note that during the production process errors may be discovered which could affect the content, and all legal disclaimers that apply to the journal pertain.



## Prussian blue nanocubes supported on graphene foam as superior binder-free anode of lithium-ion batteries

Meizhou Zhu <sup>a</sup>, Hu Zhou <sup>a,\*</sup>, Jinxiao Shao <sup>a</sup>, Jianhui Feng <sup>b</sup>, Aihua Yuan <sup>b,c,\*</sup>

<sup>a</sup> *School of Material Science and Engineering, Jiangsu University of Science and Technology, Zhenjiang, Jiangsu 212003, China*

<sup>b</sup> *School of Environmental and Chemical Engineering, Jiangsu University of Science and Technology, Zhenjiang, Jiangsu 212003, China*

<sup>c</sup> *Marine Equipment and Technology Institute, Jiangsu University of Science and Technology, Zhenjiang, Jiangsu 212003, China*

\* Corresponding authors. Tel.: +86 511 85639001.

E-mail address: zhmia119@sina.com (H. Zhou), aihua.yuan@just.edu.cn (A. H. Yuan).

**Abstract:** The integration of active materials into graphene foam (GF) is of fundamental importance for developing superior binder-free electrodes. In the present design, Prussian blue (PB) nanocubes were uniformly grown into the GF network by a facile immersion approach. This is the first example of GF supported metal cyanides and their applications as electrode materials. The as-prepared PB and GF/PB samples have been characterized systematically. This free-standing and flexible GF/PB composite electrode exhibited a high reversible gravimetric (areal) capacity of 514 mAh g<sup>-1</sup> (0.47 mAh cm<sup>-2</sup>) at 100 mA g<sup>-1</sup> over 150 cycles and superior cycling stability with 99% capacity retention as well as good rate capability of ~150 mAh g<sup>-1</sup> at 1 A g<sup>-1</sup>. Such outstanding electrochemical behaviors were attributed to the synergistic integration of both GF and PB components. Thus, the GF/PB system can be employed as potential superior binder-free anode candidates for high-performance lithium-ion batteries.

**Keywords:** Prussian blue; Graphene foam; Composite; Anode; Lithium-ion batteries

## 1. Introduction

Lithium-ion batteries (LIBs) with large power densities, high energy densities and long cyclic life are crucial to develop upgrading portable electronic devices and emerging large scale applications [1]. Metal-organic frameworks (MOFs) are a class of porous materials constructed through metal ions and organic ligands [2]. Recently, MOFs have been widely employed as electrode materials for LIBs, in which the open framework structures allow the highly reversible intercalation/extraction of ions [3-5].

Metal hexacyanoferrates (HCFs) with three-dimensional open framework, known as Prussian blue (PB) or its analogues (PBAs), have received considerable concerns as one type of crystalline MOFs applied in various fields such as magnetism, gas storage, medicine, owing to their excellent activities, low cost, high stabilities and superior environmental benignancies [6-10]. It's worth noting that the ability of metal HCFs intercalating alkali metal ions in reversible redox reactions during the charge/discharge process has rendered them to be used as electrode materials for rechargeable batteries, sensors and supercapacitors [11-15]. They have exhibited potential two-electron redox capacity and fast intercalation kinetics. Particularly, the open-framework contains large octahedral interstitial sites and open channels for ionic diffusion, which allow the insertion/extraction of alkali metal cations without collapse of the crystal framework.

However, there are still some points to be noted for the metal HCFs system. Most work on metal cyanides focused on their cathode behaviors for secondary batteries, and there are very limited examples of metal cyanides as anode materials for LIBs [16-20]. In addition, the intrinsic poor electronic conductivity of metal cyanides and inefficient electron and ion transport in the whole electrodes have largely compromise the electrochemical performances, especially in the rapid response and long-term cycling stability. The high solubility of redox intermediates and the difficulty of controlling bulk precipitation further increase the challenge of employing metal cyanides as electrode materials.

Current collector materials have played a key role in determining the utilization efficiency of active components. The traditional electrode preparation approach would easily lead to the “dead area” of active materials by mixing the electroactive components with non-conductive binder and then deposit on the metallic foil or foam. Nowadays, a promising strategy to improve electrochemical properties of metal cyanides is to utilize conductive current collectors to form hybrids, and several candidates have been considered as electrode substrates to support PBAs active materials. For instance, Hao et al. deposited Ni-HCF nanocubes on flexible carbon fibers by an electro-deposition method, and the resulting electrode displayed remarkable electrochemical performances in the neutral electrolyte [21]. Fu et al successfully prepared flower-like Ni-HCF nanosheets coated 3D hierarchical porous Ni film, and the areal specific capacitance was 10 times larger than that of Ni-HCF deposited on smooth Ni film [22]. Wu et al. fabricated Co-HCF and Ni-HCF nanostructures with graphene-coated stainless steel through a solution co-precipitation process, showing superior supercapacitive properties [23]. As we all know, compared with the layered graphene or graphene oxide [24, 25], graphene foam (GF) with three-dimensional architecture has the potential to serve as an excellent current collector in the energy field because of its intriguing properties, especially the rapid mass and electron transport kinetics for alkali metal cations [26, 27]. GF decorated with various active materials have been used directly as binder-free electrodes of rechargeable batteries, and showed superior activities relative with those of pure components [28]. Motivated by the merits of metal cyanides and GF, it can be anticipated that the GF/metal cyanide hybrids as binder-free electrodes would exhibit intriguing electrochemical performances.

In the previous studies, our group has described an approach to prepare GF/metal oxides hierarchical composites, and the obtained free-standing GF/Mn<sub>2</sub>O<sub>3</sub> and GF/CuO electrodes had high gravimetric and areal capacities, good rate capacities and superior cycling behaviors [29, 30]. Along with this line, herein we developed a simple route to prepare GF supported PB with the chemical formula FeFe(CN)<sub>6</sub>, in which PB nanocubes are in-situ grown on the GF surface and interconnected with 3D

conductive nanostructure scaffold. The isolating GF/PB composites were used as free-standing anode electrodes of LIBs, delivering superior electrochemical properties relative with pristine PB and GF. To the best of our knowledge, there were no examples until now on the rational design and synthesis of GF decorated with metal cyanides for energy applications. The excellent electrochemical behaviors were reasonably attributed to the synergistic interaction between highly active PB nanocubes and the conductive GF with interconnected porous network.

## 2. Experimental details

### 2.1 Materials

All chemical reagents were purchased from Sigma-Aldrich and used without further purification. Graphene foam (GF) was synthesized by a chemical vapor deposition method reported previously [31].

### 2.2 Syntheses of PB and GF/PB

PB nanocubes were prepared by a chemical precipitation approach according to the literature [32]. Typically, an aqueous solution of  $K_3Fe(CN)_6$  (50 mL, 0.1 M) was added dropwise to an aqueous solution of  $FeCl_3$  (100 mL, 0.1 M) with continuous stirring, and then the solution was further stirred at 60 °C for 12 h. The resulting precipitates were collected by centrifugation, washed with deionized water three times. After the products were dried in a vacuum oven at 60 °C overnight,  $FeFe(CN)_6$  (PB) particles were generated. The GF/PB sample was prepared through a facile impregnation approach described as follows. A piece of GF (1 cm × 1 cm) was treated with acid and putted gently into a glass bottle. An aqueous solution of  $K_3Fe(CN)_6$  (2 mL, 0.1 M) was added into the bottle, followed by adding dropwise an aqueous solution of  $FeCl_3$  (4 mL, 0.1 M). The bottle was shaken slowly for 30 seconds and kept at 60 °C for 12 h. The resulting product was washed three times with deionized water, and dried under vacuum at 60 °C overnight.

### 2.3 Physical characterization

X-ray diffraction (XRD) patterns of all samples were collected with a Shimadzu XRD-6000 diffractometer using  $Cu-K\alpha$  radiation ( $\lambda = 1.5406 \text{ \AA}$ ). X-ray photoelectron spectra (XPS) were conducted using a Thermo-Fisher Scientific ESCALAB 250 Xi (Al- $K\alpha$

achromatic X-ray source). The microstructures were observed by field-emission scanning electron microscopy (FE-SEM, ZEISS Merlin Compact) and transmission electron microscopy (FE-TEM, JEOL JEM-2100F). The elemental mapping analysis was investigated with an energy-dispersive X-ray spectrometry (EDS, Oxford X-Max). Raman spectra were obtained on a Digilab FTS-3500 (Bio-Rad) using an Ar ion laser with a wavelength of 532 nm.

#### 2.4 Electrochemical measurement

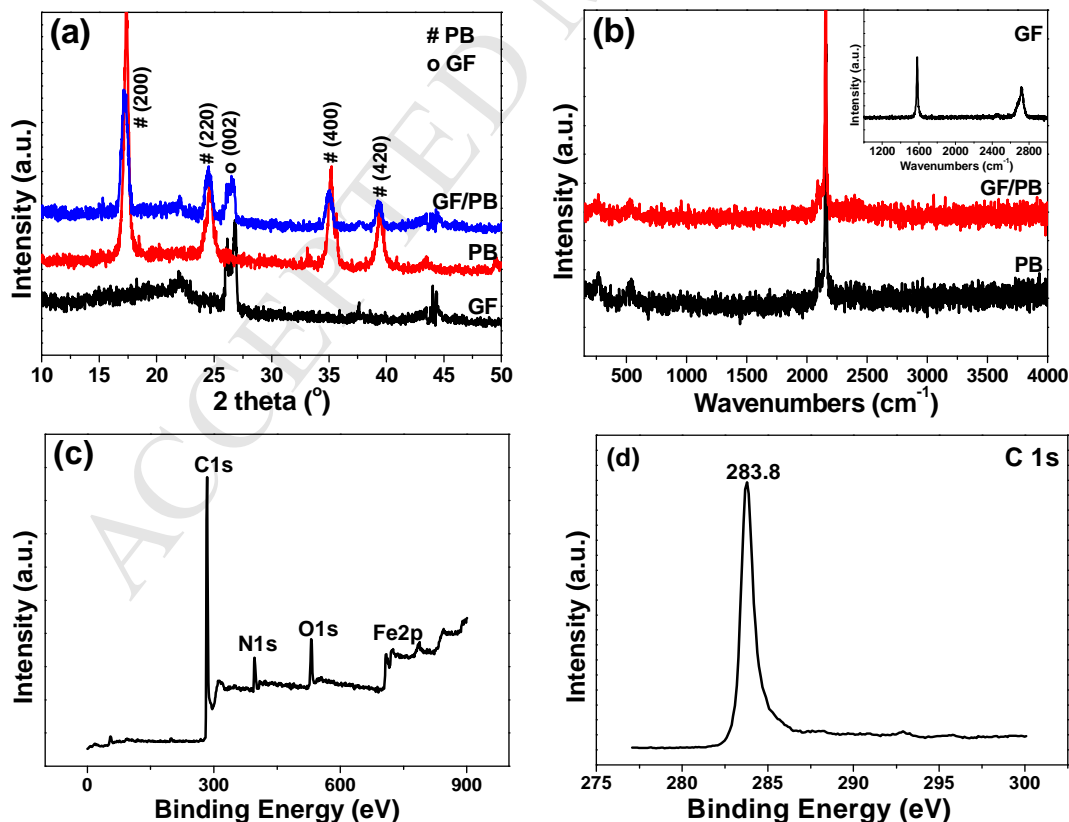
Electrochemical performances of the products were evaluated in CR2032-type coin cells, which were assembled in an Ar-filled glovebox with water/oxygen level lower than 1 ppm. 1.0 M LiPF<sub>6</sub> in ethylene carbonate/diethyl carbonate (1:1 in volume) was employed as the electrolyte and Celgard 2600 membrane acted as the separator. The PB, GF and GF/PB materials were used as the working electrodes, whereas lithium foil acted as the counter electrode. The working electrode for pure PB was prepared by tape-casting a slurry of 70 wt% active material PB, 20 wt% conductive carbon black and 10 wt% polyvinylidene fluoride (PVDF) binder onto copper foil, and then dried at 60 °C under vacuum for 12 h. Both the GF and GF/PB samples can be employed directly as working electrodes due to their free-standing feature. Galvanostatic charge-discharge experiments were conducted on a LAND CT 2001A battery test system with a voltage window of 0.01-3.0 V. Electrochemical impedance spectroscopy (EIS) was performed on an Autolab system (Metrohm) over the frequency range of 0.1-100 kHz with an amplitude of 5 mV.

### 3. Results and discussion

#### 3.1. Powder X-ray diffraction and Raman spectra

Fig. 1a presented XRD patterns of the GF, PB and GF/PB samples. The obvious diffraction peak observed at about  $2\theta = 26.5^\circ$  for GF was assigned to the (0 0 2) plane of graphitic carbon (JCPDS card no. 75-1621). The patterns of pure PB can be well indexed to the face-centered cubic lattice (JCPDS card no. 73-0687), where the diffraction peaks at  $2\theta = 17.4, 24.8, 35.3$  and  $39.5^\circ$  corresponded to the (200), (220), (400) and (420) planes, respectively. In the XRD patterns of GF/PB, the diffraction

peaks of both the GF and PB components can be obviously seen, which further validated the successful loading of PB particles on the GF surface. The wide diffraction peaks for PB phase probably suggested the small crystalline size of particles. Raman spectra of PB and GF/PB were shown in Fig. 1b, in which two obvious peaks observed at 1582 and 2688  $\text{cm}^{-1}$  for GF were assigned to the G and 2D signals, respectively. The 2D and G bands are attributed to the disordered carbon arising from structural defects and tangential C-C stretching vibrations, respectively [33]. The relatively low integral ratio of G to 2D band indicated the presence of few-layered graphene sheets in GF [34]. For the GF/PB samples, the presence of bands assigned to PB after PB formation can be observed at 267 and 532  $\text{cm}^{-1}$  (Fe-C stretching), and at 2093 and 2151  $\text{cm}^{-1}$  (C $\equiv$ N stretching) [35, 36]. The corresponding GF peaks were not detected in the spectrum for the composite, which can be probably ascribed to the fact that the surface of GF was covered completely by a large amount of PB particles, which can be demonstrated by the following morphological analysis.



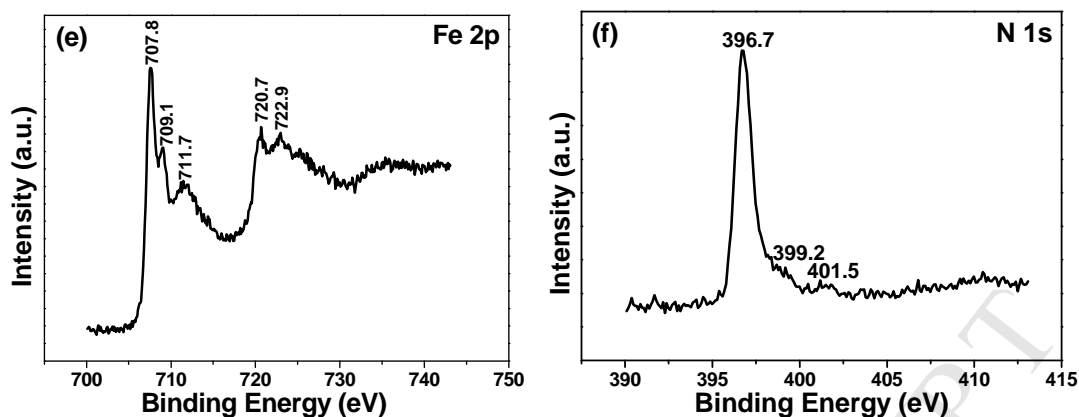


**Fig. 1** (a) XRD patterns of as-prepared GF, PB, and GF/PB samples; (b) Raman spectra of PB and GF/PB; XPS (c) survey, (d) C 1s, (e) Fe 2p, and (f) N 1s spectra of GF/PB.

### 3.2. X-ray photoelectron spectra

The surface elemental makeup and oxidation states were investigated using XPS (Figs. 1c-1f). The survey spectrum of GF/PB demonstrated the presence of C1s, N1s, O1s, and Fe2p peaks without any impurities. The oxygen peak mainly originated from those adsorbed water molecules. The obvious peak at 283.8 eV was attributed to the  $sp^2$ -hybridized carbon atoms from GF [37]. To further explore the electronic states of each element, more attention has been paid to the high-resolution spectra of Fe and N. In the Fe2p spectrum, the binding energies at 709.1 eV and 722.9 eV originated from  $Fe^{III} 2p_{3/2}$  and  $Fe^{III} 2p_{1/2}$  of  $[Fe^{III}(CN)_6]$  in the PB framework, whereas the peak at 711.7 eV was attributed to  $Fe^{III} 2p_{3/2}$  coordinated to nitrogen atom. Two peaks at 707.8 eV and 720.7 eV were ascribed to  $Fe^{II} 2p_{3/2}$  and  $Fe^{II} 2p_{1/2}$  of  $[Fe^{II}(CN)_6]$  in PB [31,38,39], respectively. In the N1s spectrum, the core-level spectrum of N1s had three peaks at 401.5, 399.2 and 396.7 eV, confirming the presence of  $C\equiv N$  in the composite. The XPS analysis of Fe2p and N1s spectra confirmed the successful growth of PB particles in the GF substrate.

### 3.3. Morphologies

The microstructures of GF, PB and GF/PB were analyzed by SEM. GF displayed a typical 3D porous network (Fig. 2a), while PB particles showed uniform and well-packed nanocubes (Fig. 2b) [32]. For the GF/PB composite, the entire skeleton of GF was wrapped densely by PB crystals and the GF surface was rough (Fig. 2c, Fig.

2d). Notably, PB nanocubes in GF/PB presented less aggregation and appeared more regular because of the confinement of GF as well as the intimate contact between PB and GF. Actually, the interpenetrated porous feature of GF provided a highly accessible area, and effectively prevented the aggregation of PB particles, while the remarkable electronic conductivity of GF was beneficial to rapidly transport and diffuse electrolyte ions/electrons upon charging/discharging [40-42]. During PB loading process, the color of GF gradually changed from black to blue, implying in-situ decoration of PB particles. As shown in Fig. 2e, the corresponding elemental mapping images of GF/PB demonstrated the uniform distribution of Fe, C and N throughout the whole sample, indicating the successful deposition of PB particles into the GF network.

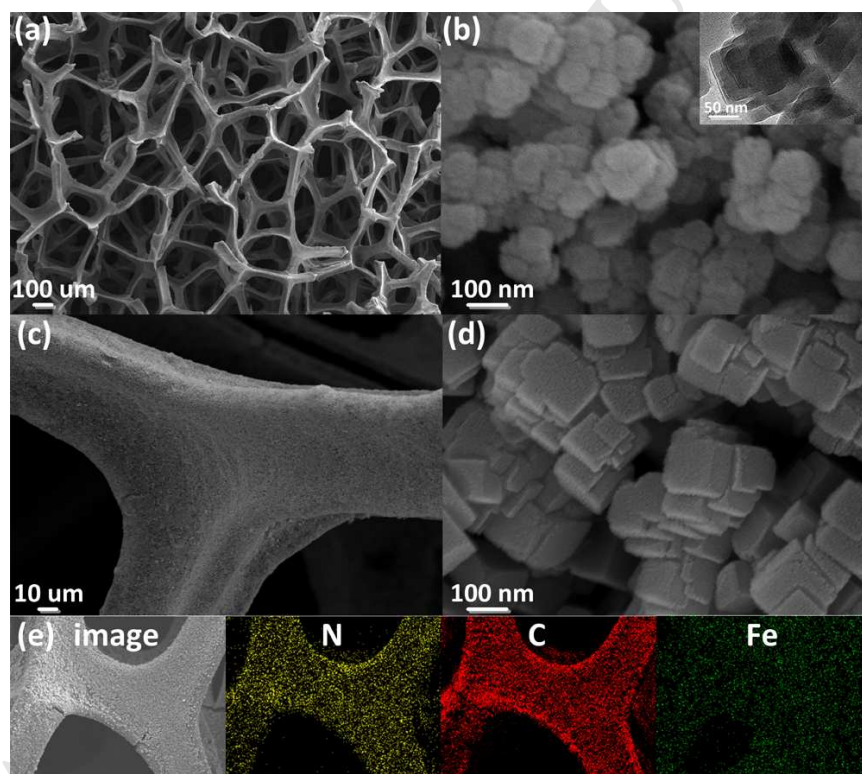


**Fig. 2** SEM images of (a) GF, (b) PB (inset: TEM image of PB), and (c, d) GF/PB; (e) EDS elemental mapping showing the spatial distribution of C, N and Fe species for GF/PB.

### 3.4. Electrochemical performances

The charge-discharge curves of the GF/PB electrode were shown in Fig. 3a. The first discharge and charge capacities were 578.7 and 385.0 mAh g<sup>-1</sup> (areal capacities of 0.53 and 0.35 mAh cm<sup>-2</sup>), respectively, exhibiting a columbic efficiency of about

67%. The subsequent coulombic efficiency slightly increased to 95% and 99% in the 2nd and 50th cycles, respectively, yielding a high cycling stability. The cycling performances of PB and GF/PB at  $100 \text{ mA g}^{-1}$  were shown in Fig. 3b. Obviously, the GF/PB electrode exhibited a superior capacity retention ability and cycling stability than those of pure PB over 150 cycles and GF over 50 cycles (Fig. S1). For pure PB, the second discharge capacity was  $645.3 \text{ mAh g}^{-1}$  after a large capacity loss in the first cycle, followed by the gradual decrease to  $299.8 \text{ mAh g}^{-1}$  (150 cycles). The severe capacity decay of PB was ascribed to the agglomeration and pulverization of nanocubes during the cycling process [43]. By contrast, the composite electrode displayed a high cycle stability and the capacity raised slightly upon the discharging-charging cycles and still remained to  $514 \text{ mAh g}^{-1}$  (a large areal capacity of  $0.47 \text{ mAh cm}^{-2}$ ) at  $100 \text{ mA g}^{-1}$  after 150 cycles.

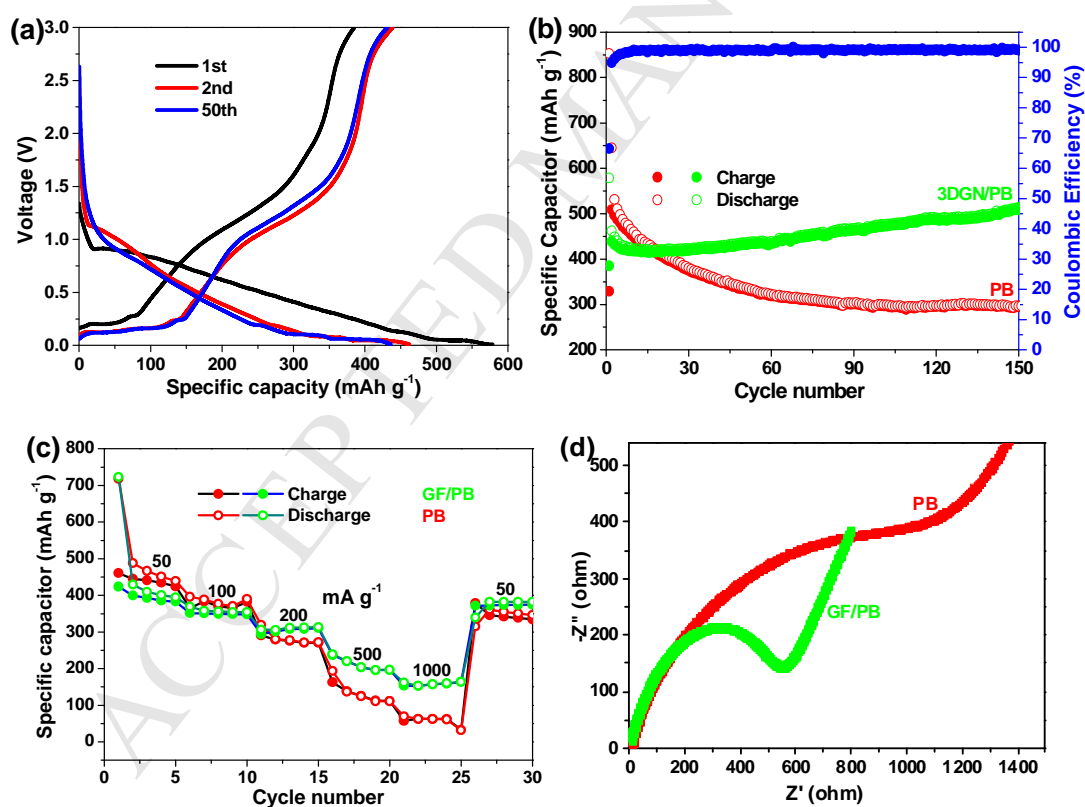


**Fig. 3** (a) Charge-discharge curves of GF/PB at a current density of  $100 \text{ mA g}^{-1}$ ; (b) The cycling performance of PB and GF/PB at  $100 \text{ mA g}^{-1}$ ; (c) The rate performance of PB and GF/PB at different current densities from 50 to  $1000 \text{ mA g}^{-1}$ ; (d) Nyquist plots of PB and GF/PB.

In order to carry out the controlled experiments, two GF/PB composites with low and high PB loadings were prepared and characterized by morphologically. It can be found that excessive PB particles aggregated seriously on the surface of GF when PB loading was high (3 times the initial content), while the surface of GF have not been completely covered by PB particles for the low-loading sample (1/5 times the initial content) (Fig. S2). Electrochemical studies revealed that the moderate PB loading was crucial to the improvement of lithium storage properties, while the much low or high loadings of PB will have negative effect on the electrochemical performances of the composites (Fig. S3). The contribution of PB component to lithium storage decreased when the loading of PB is low, resulting in the poor specific capacity of the corresponding composite. The cycling curve of this composite went stabilized after 50 cycles with the specific capacity of  $\sim 380 \text{ mAh g}^{-1}$ , close to the value of pure GF. In contrast, the high PB content led to the decay in the cycling life, although slightly enhanced capacities were observed at initial several cycles. The capacity decay for this composite can be ascribed to the following fact: 1) the conductivity for the composite undoubtedly decreased in the presence of excess PB particles, restricting the fast transfer of electrons/ions during the discharge/charge process; 2) those outermost excessive PB particles on the GF surface probably separated from the GF substrate and then dissolved into the electrolyte due to their weak binding interactions to the substrate upon cycling. Thus, the specific capacity of this composite continuously declined to about  $402 \text{ mAh g}^{-1}$  after 50 cycles.

In general, the reported PBAs generally exhibited severe or slight capacity decays with increasing cycling numbers [16-20]. Notably, the gradual increase in capacity was observed in our case. Thus, the 3DGN/PB electrode in the present work keeps obvious advantages in lithium storage compared to these PBAs anodes and even GF/MOF-derived CuO in the aspects of specific capacitances and long-term cycling stabilities (Table 1). The intriguing electrochemical performance can be attributed to the intrinsic characteristics for such system: 1) the porous structure of GF can serve as an elastic and stable buffer effectively alleviating and accommodating volume changes with PB particles during the insertion/exaction process of lithium ions, which was commonly observed in GF-based anode materials [44]; 2) the unique GF/PB

binder-free structure provided open interspaces and electrochemically active surface, and thus showed higher adsorption/desorption capacities for lithium ions; 3) The encapsulation arrangement with the 3D interconnected graphene architecture can provide continuous pathways and extensive diffusion channels for the transport of electron and lithium ion through the overall electrode, significantly enhancing electrical conductivity and lithium insertion/extraction kinetics of the electrode. So, the proposed GF/PB electrode exhibited better rate capability compared with PB. Furthermore, the Coulombic efficiency of the GF/PB composite still remained at almost 100% after 150 cycles, revealing the fast stabilization of SEI layer as well as high reversibility for the conversion reaction of lithium and anode material. The significantly improved capacity was ascribed to the synergistic effect of GF and PB components.

**Table 1.** Comparison of specific capacities of the GF/PB composite with reported PBAs anodes for LIBs.

Electrode materials	Current density (mA g <sup>-1</sup> )	Cycle number	Specific capacity (mAh g <sup>-1</sup> )	Refs
GF/PB	100	150	514	this work
Ti <sub>0.75</sub> Fe <sub>0.25</sub> [Fe(CN) <sub>6</sub> ] <sub>0.96</sub> · 1.9H <sub>2</sub> O	350	100	127	16
Mn[Fe(CN) <sub>6</sub> ] <sub>0.6667</sub> ·nH <sub>2</sub> O	100	20	~540	17
K <sub>1-x</sub> Fe <sub>2+x/3</sub> (CN) <sub>6</sub> ·yH <sub>2</sub> O	8.75	50	400	18
Mn <sub>3</sub> [Co(CN) <sub>6</sub> ] <sub>2</sub> ·nH <sub>2</sub> O	50	100	35.3	19
Co <sub>3</sub> [Co(CN) <sub>6</sub> ] <sub>2</sub> ·nH <sub>2</sub> O	20	5	~300	19
Co <sub>3</sub> [Fe(CN) <sub>6</sub> ] <sub>2</sub> ·nH <sub>2</sub> O	100	30	325	20
GF/CuO	100	50	405	29

There are no obvious differences in specific capacities between GF/PB and PB electrodes at low current densities (50 and 100 mA g<sup>-1</sup>), as shown in Fig. 3c. In comparison, GF/PB exhibited a better rate performance than PB when the current densities further increased from 200-1000 mA g<sup>-1</sup>. The capacity of GF/PB was about

150 mAh g<sup>-1</sup> even at 1 A g<sup>-1</sup>, compared to 60 mAh g<sup>-1</sup> observed for PB at the same current density. The specific capacity of GF/PB remained 382 mAh g<sup>-1</sup> with the current density returning to 50 mA g<sup>-1</sup>, demonstrating the structural stability for the composite electrode during the cycling process. To evaluate the kinetics of electrochemical reactions on the electrodes, electrochemical impedance spectroscopy (EIS) of PB and GF/PB samples was carried out, as shown in Fig. 3d. It can be found from Nyquist plots that the bulk solution resistance of GF/PB was much smaller than that of PB because of the introduction of conductive GF substrate, as found in these GF/metal oxides [45, 46]. In our case, the strong coupling and intact contact between PB particles and conductive GF substrate can facilitate the rapid electron/charge transfer and accelerate the reaction kinetics of lithium storage, which is beneficial for the improvement of high-rate capability of the GF/PB anode. To further explore the mechanism of cycling stabilities, the microstructures of PB and GF/PB after 50 cycles were performed, as shown in Fig. S4. The obvious pulverization and aggregation of particles for the PB electrode was observed, and then part of these particles will separate from the current collector and then dissolve into the electrolyte, resulting in the continuous decrease of capacity upon cycling. However, PB particles have refined into much smaller ones after cycling for the GF/PB composite electrode. Accordingly, the binding force between these refined PB nanoparticles and GF substrate was further strengthened, which improved the structural stability and then the cycling stability of the whole electrode. For the GF/PB electrode, the charge transfer resistance after 150 cycles was significantly smaller than that before cycling (Fig. S5), which originated from the more close contact between these refined PB particles and GF substrate as well as the uniform dispersion of PB nanoparticles on the surface of GF, increasing the electronic conductivity.

#### 4. Conclusions

In summary, we have successfully developed a facile and controllable approach fabricating the GF/PB composite system. The resulting GF/PB material was applied as light-weight and free-standing electrode for LIBs. It is important to highlight here that

the composite electrode not only exhibited high gravimetric and areal capacities, but also delivered an excellent long-term cycling performance and rate capacity. The superior electrochemical properties than individual components originated from the synergistic integration of GF and PB components. The large open space of the unique structure offered tunnels and space for the transport and storage of lithium ions. This is the first demonstration of the design and preparation of GF supported metal cyanides and their applications as electrode materials. The present synthetic strategy may be extended to different kinds of GF/MOF hybrids for constructing cost-effective, environmentally friendly and high-performance LIBs for energy applications.

### Acknowledgments

This work was supported by National Natural Science Foundation (51672114), Natural Science Foundation of Jiangsu Province (BK20151328, BK20161357), Foundation from Marine Equipment and Technology Institute for Jiangsu University of Science and Technology (HZ20170015), and the project of the Priority Academic Program Development of Jiangsu Higher Education Institutions.

### References

- [1] M. Armand, J.M. Tarascon, Building better batteries, *Nature* 451 (2008) 652-657.
- [2] H. Furukawa, K.E. Cordova, M. O’Keeffe, O.M. Yaghi, The chemistry and applications of metal-organic frameworks, *Science* 341 (2013) 1230444.
- [3] L. Wang, Y.Z. Han, X. Feng, J.W. Zhou, P.F. Qi, B. Wang, Metal-organic frameworks for energy storage: Batteries and supercapacitors, *Coord. Chem. Rev.* 307 (2016) 361-381.
- [4] Y.Y. Chen, Y. Wang, H.X. Yang, H. Gan, X.W. Cai, X.M. Guo, B. Xu, M.F. Lv, A.H. Yuan, Facile synthesis of porous hollow  $\text{Co}_3\text{O}_4$  microfibers derived-from metal-organic frameworks as an advanced anode for lithium ion batteries, *Ceramics Inter.* 43 (2017) 9945-9950.
- [5] L.M. Zhang, B. Yan, J.H. Zhang, Y.J. Liu, A.H. Yuan, G. Yang, Design and self-assembly of metal-organic framework-derived porous  $\text{Co}_3\text{O}_4$  hierarchical structures for lithium-ion batteries, *Ceramics Inter.* 42 (2016) 5160-5170.
- [6] L. Catala, T. Mallah, Nanoparticles of Prussian blue analogs and related

- coordination polymers: From information storage to biomedical applications, *Coord. Chem. Rev.* 346 (2017) 32-61.
- [7] A. Paoella, C. Faure, V. Timoshevskii, S. Marras, G. Bertoni, A. Guerfi, A. Vijn, M. Armand, K. Zaghib, A review on hexacyanoferrate-based materials for energy storage and smart windows: Challenges and perspectives, *J. Mater. Chem. A* 5 (2017) 18919-18932.
- [8] C.R. Patra, Prussian blue nanoparticles and their analogues for application to cancer theranostics, *Nanomedicine* 11 (2016) 569-572.
- [9] G.N. Newton, M. Nihei, H. Oshio, Cyanide-bridged molecular squares - the building units of Prussian blue, *Eur. J. Inorg. Chem.* (2011) 3031-3042.
- [10] S.S. Kaye, J.R. Long, Hydrogen storage in the dehydrated Prussian blue analogues  $M_3[Co(CN)_6]_2$  (M = Mn, Fe, Co, Ni, Cu, Zn), *J. Am. Chem. Soc.* 127 (2005) 6506-6507.
- [11] F. Ma, Q. Li, T.Y. Wang, H.G. Zhang, G. Wu, Energy storage materials derived from Prussian blue analogues, *Sci. Bull.* 62(2017) 358-368.
- [12] H. Pang, Y.Z. Zhang, T. Cheng, W.Y. Lai, W. Huang, Uniform manganese hexacyanoferrate hydrate nanocubes featuring superior performance for low-cost supercapacitors and nonenzymatic electrochemical sensors, *Nanoscale* 7 (2015) 16012-16019.
- [13] D.W. Su, M. Cortie, H.B. Fan, G.X. Wang, Prussian blue nanocubes with an open framework structure coated with PEDOT as high-capacity cathodes for lithium-sulfur batteries, *Adv. Mater.* (2017) 1700587.
- [14] L. Wang, Y.H. Lu, J. Liu, M.W. Xu, J.G. Cheng, D.W. Zhang, J.B. Goodenough, A superior low-cost cathode for a Na-ion battery, *Angew. Chem. Int. Ed.* 52 (2013) 1964-1967.
- [15] C.D. Wessells, R.A. Huggins, Y. Cui, Copper hexacyanoferrate battery electrodes with long cycle life and high power, *Nat. Commun.* 2 (2011) 550.
- [16] X. Sun, X.Y. Ji, Y.T. Zhou, Y. Shao, Y. Zang, Z.Y. Wen, C.H. Chen, A new gridding cyanoferrate anode material for lithium and sodium ion batteries:  $Ti_{0.75}Fe_{0.25}[Fe(CN)_6]_{0.96} \cdot 1.9H_2O$  with excellent electrochemical properties, *J.*

- Power Sources 314 (2016) 35-38.
- [17] P.X. Xiong, G.J. Zeng, L.X. Zeng, M.D. Wei, Prussian blue analogues  $\text{Mn}[\text{Fe}(\text{CN})_6]_{0.6667} \cdot n\text{H}_2\text{O}$  cubes as an anode material for lithium-ion batteries, Dalton Trans. 44 (2015) 16746-16751.
- [18] M. Piernas-Munoz, E. Castillo-Martinez, V. Roddatis, M. Armand, T. Rojo,  $\text{K}_{1-x}\text{Fe}_{2+x/3}(\text{CN})_6 \cdot y\text{H}_2\text{O}$ , Prussian blue as a displacement anode for lithium ion batteries, J. Power Sources 271 (2014) 489-496.
- [19] P. Nie, L.F. Shen, H.F. Luo, B. Ding, G.Y. Xu, J. Wang, X.G. Zhang, Prussian blue analogues: a new class of anode materials for lithium ion batteries, J. Mater. Chem. A 2 (2014) 5852-5857.
- [20] M. Shokouhimehr, S.H. Yu, D.C. Lee, D.S. Ling, T. Hyeon, Y.E. Sung, Metal hexacyanoferrate nanoparticles as electrode materials for lithium ion batteries, Nanosci. Nanotechnol. Lett. 5 (2013) 770-774.
- [21] X.L. Ma, X. Du, X.M. Li, X.G. Hao, A.D. Jagadale, A. Abudula, G.Q. Guan, In situ unipolar pulse electrodeposition of nickel hexacyanoferrate nanocubes on flexible carbon fibers for supercapacitor working in neutral electrolyte, J. Alloy. Compd. 695 (2017) 294-301.
- [22] H. Jiang, Y.T. Xu, T. Wang, P.L. Zhu, S.H. Yu, Y. Yu, X.Z. Fu, R. Sun, C.P. Wong, Nickel hexacyanoferrate flower-like nanosheets coated three dimensional porous nickel films as binder-free electrodes for neutral electrolyte supercapacitors, Electrochim. Acta 166 (2015) 157-162.
- [23] M.S. Wu, L.J. Lyu, J.H. Syu, Copper and nickel hexacyanoferrate nanostructures with graphene-coated stainless steel sheets for electrochemical supercapacitors, J. Power Sources 297 (2015) 75-82.
- [24] Y.C. Hao, D.B. Xiong, W. Liu, L.L. Fan, D.J. Li, X.F. Li, Controllably designed "vice-electrode" interlayers harvesting high performance lithium sulfur batteries, ACS Appl. Mater. Interfaces 9 (2017) 40273-40280.
- [25] M. Yang, X.F. Li, B. Yan, L.L. Fan, Z.X. Yu, D.J. Li, Reduced graphene oxide decorated porous  $\text{SnO}_2$  nanotubes with enhanced sodium storage, J. Alloy. Compd. 710 (2017) 323-330.

- [26] L.L. Fan, X.F. Li, X.S. Song, N.N. Hu, D.B. Xiong, A. Koo, X.L. Sun, Promising dual-doped graphene aerogel/SnS<sub>2</sub> nanocrystal building high performance sodium ion batteries, *ACS Appl. Mater. Interfaces* 10 (2017) 2637-2648.
- [27] X.H. Xia, D.L. Chao, Y.Q. Zhang, Z.X. Shen, H.J. Fan, Three-dimensional graphene and their integrated electrodes, *Nano Today* 9 (2014) 785-807.
- [28] B. Luo, L.J. Zhi, Design and construction of three dimensional graphene-based composites for lithium ion battery applications, *Energy Environ. Sci.* 8 (2015) 456-477.
- [29] D. Ji, H. Zhou, Y.L. Tong, J.P. Wang, M.Z. Zhu, T.H. Chen, A.H. Yuan, Facile fabrication of MOF-derived octahedral CuO wrapped 3D graphene network as binder-free anode for high performance lithium-ion batteries, *Chem. Eng. J.* 313 (2017) 1623-1632.
- [30] D. Ji, H. Zhou, J. Zhang, Y.Y. Dan, H.X. Yang, A.H. Yuan, Facile synthesis of a metal-organic framework-derived Mn<sub>2</sub>O<sub>3</sub> nanowire coated three-dimensional graphene network for high-performance free-standing supercapacitor electrodes, *J. Mater. Chem. A* 4 (2016) 8283-8290.
- [31] X.H. Cao, Y.M. Shi, W.H. Shi, G. Lu, X. Huang, Q.Y. Yan, Q.C. Zhang, H. Zhang, Preparation of novel 3D graphene networks for supercapacitor applications, *Small* 7 (2011) 3163-3168.
- [32] X.Y. Wu, Y. Luo, M.Y. Sun, J.F. Qian, Y.L. Cao, X.P. Ai, H.X. Yang, Low-defect Prussian blue nanocubes as high capacity and long life cathodes for aqueous Na-ion batteries, *Nano Energy* 13 (2015) 117-123.
- [33] A.C. Ferrari, J. Robertson, Interpretation of Raman spectra of disordered and amorphous carbon, *Phys. Rev. B* 61 (2000) 14095-14107.
- [34] D. Graf, F. Molitor, K. Ensslin, C. Stampfer, A. Jungen, C. Hierold, L. Wirtz, Spatially resolved Raman spectroscopy of single-and few-layer graphene, *Nano Lett.* 7 (2007) 238-242.
- [35] R. Mažeikienė, G. Niaura, A. Malinauskas, Electrocatalytic reduction of hydrogen peroxide at Prussian blue modified electrode: An in situ Raman spectroelectrochemical study, *J. Electroanal. Chem.* 660 (2011) 140-146.

- [36] K. Nakamoto, in: Infrared and Raman spectra of inorganic and coordination compounds. John Wiley & Sons Inc. (2008) 1-147.
- [37] G.D. Ruan, Z.Z. Sun, Z.W. Peng, J.M. Tour, Growth of graphene from food, insects, and waste, *ACS Nano* 5 (2011) 7601-7607.
- [38] S. Manivannan, I. Kang, K. Kim, In situ growth of Prussian blue nanostructures at reduced graphene oxide as a modified platinum electrode for synergistic methanol oxidation, *Langmuir* 32 (2016) 2890-2898.
- [39] L. Cao, Y. Liu, B. Zhang, L. Lu, In situ controllable growth of Prussian blue nanocubes on reduced graphene oxide: Facile synthesis and their application as enhanced nanoelectrocatalyst for  $H_2O_2$  reduction, *ACS Appl. Mater. Inter.* 2 (2010) 2339-2346.
- [40] G.M. Zhou, L. Li, C.Q. Ma, S.G. Wang, Y. Shi, N. Korotkar, W.C. Ren, F. Li, H.M. Cheng, A graphene foam electrode with high sulfur loading for flexible and high energy Li-S batteries, *Nano Energy* 11 (2015) 356-365.
- [41] J. Wang, J.L. Liu, D.L. Chao, J.X. Yan, J.Y. Lin, Z.X. Shen, Self-assembly of honeycomb-like  $MoS_2$  nanoarchitectures anchored into graphene foam for enhanced lithium-ion storage, *Adv. Mater.* 26 (2014) 7162-7169.
- [42] J.S. Luo, J.L. Liu, Z.Y. Zeng, C.F. Ng, L.J. Ma, H. Zhang, J.Y. Lin, Z.X. Shen, H.J. Fan, Three-dimensional graphene foam supported  $Fe_3O_4$  lithium battery anodes with long cycle life and high rate capability, *Nano Lett.* 13 (2013) 6136-6143.
- [43] J.J. Zhang, A.S. Yu, Nanostructured transition metal oxides as advanced anodes for lithium-ion batteries, *Sci. Bull.* 60 (2015) 823-838.
- [44] J.Y. Ji, Y. Li, W.C. Peng, G.L. Zhang, F.B. Zhang, X.B. Fan, Advanced graphene-based binder-free electrodes for high-performance energy storage, *Adv. Mater.* 27 (2015) 5264-5279.
- [45] S.H. Choi, J.K. Lee, Y.C. Kang, Three-dimensional porous graphene-metal oxide composite microspheres: Preparation and application in Li-ion batteries, *Nano Research* 8 (2015) 1584-1594.
- [46] W. Wei, S.B. Yang, H.X. Zhou, I. Lieberwirth, X.L. Feng, K. Müllen, 3D graphene foams cross-linked with pre-encapsulated  $Fe_3O_4$  nanospheres for enhanced

lithium storage, Adv. Mater. 25 (2013) 2909-2914.

ACCEPTED MANUSCRIPT

**Highlights**

1. A facile strategy to fabricate graphene foam (GF) supported metal cyanides was proposed.
2. GF/metal cyanides were prepared and used as electrode materials for the first time.
3. The binder-free electrode showed excellent electrochemical performances of LIBs.